A Study of Strain and Electric Field Induced Photocatalytic Crossover in g-C_3N_4/CoN_4 Nanocomposite through DFT : Upgradation from Type-I to Type-II Photocatalyst for Water Splitting Reaction

Dhilshada. V. N[a], Sabyasachi Sen[b], Mausumi Chattopadhyaya[a]*

[a] *Department of Chemistry, National Institute of Technology, Calicut, Calicut Mukkam Road, Kattangal, Kerala 673601, India*

[b] *Department of Physics, Shyampur Siddheswari Mahavidyalaya, Ajodhya, Shyampur, Howrah, Pin-711312& JIS College of Engineering Block A, Phase-III, Kalyani, Nadia, PIN-741235, India*

Abstract

Van der Waals (vdW) heterojunctions, consisting of two-dimensional monolayers, represent a recent category of materials characterized by their highly adjustable band alignment, bandgap energy, and bandgap transition characteristics. In this investigation, we employed density functional theory calculations to explore the formation of a vdW heterojunction involving heptazine-based graphitic carbon nitride (g-C_3N_4) monolayer and CoN_4 (111) slab, denoted as g-C_3N_4/CoN_4. This specific heterojunction holds promise as a potential catalyst for solar-driven photocatalysis in the water-splitting reaction. Upon the creation of the heterojunction, a type-I direct bandgap (Eg = 2.00 eV) is established, featuring appropriate conduction band minimum and valence band maximum levels in relation to the oxidation/reduction potentials for the water-splitting reaction. Moreover, the band alignment, bandgap energy, and transition type of the heterojunction can be tuned finely by applying external perpendicular electric fields (±0.5 V/Å) and biaxial strains of (±6 %). Notably, a -2% strain induces a type-II band alignment (E_g = 2.1 eV, direct), while an electric field of +0.5 V/Å also results in a type-II heterostructure (E_g = 1.90 eV, direct). The state-of-the-art DFT study reveals a photocatalytic crossover in g-C_3N_4/CoN_4 from type-I to type-II in presence of bilateral strain and electric field.

Introduction

The worldwide attention on energy shortage and environmental pollution, driven by industrial development and population growth, has led to a strong desire to explore and develop clean

and renewable energy sources [1-12]. One of the key strategies is the conversion of solar energy into other valuable forms of energy through various methods, such as photocatalysis [13-16], solar cells [17], photoelectrochemical cells [18], and photothermal conversion [19]. Among these, photocatalysis stands out as the most promising approach due to its ability to use solar energy to produce valuable fuels like hydrogen, oxygen, methanol, methane, and ethanol [20-24]. Graphitic carbon nitride (g-C_3N_4)-based materials have gained considerable interest as promising photocatalysts, thanks to their ease of preparation and functionalization, attractive electronic band structure, high physicochemical stability, and good photocatalytic performance [25-27]. However, despite notable progress, the photocatalytic efficiency of conventional g-C_3N_4-based photocatalysts is still too low for practical applications due to rapid electron-hole recombination and poor light utilization efficiency [28-30]. Thus, it is crucial to explore advanced g-C_3N_4-based photocatalysts with high light utilization efficiency and effective electron-hole separation.

In order to improve the photocatalytic properties of g-C_3N_4-based photocatalysts, various techniques have been proposed, such as doping [31-32], porous architectures [33-34], highly crystalline structures [35], metal loading [36-37], and heterojunction construction [38-39]. Typically, there are three types of conventional hetero-junction photocatalysts: those with a straggling gap (Type-I), those with a staggered gap (type-II), and those with a broken gap (type-III) [40]. For the Type-I heterojunction photocatalyst, the conduction band (CB) and the valence band (VB) of semiconductor A are higher and lower, respectively, than the corresponding bands of semiconductor B [41]. As a result, under light irradiation, electrons and holes accumulate at the CB and VB levels of semiconductor B, respectively. However, since both electrons and holes accumulate on the same semiconductor, the electron-hole pairs cannot be effectively separated for the Type-I heterojunction photocatalyst. Additionally, a redox reaction occurs on the semiconductor with the lower redox potential, significantly reducing the redox ability of the heterojunction photocatalyst. On the other hand, for the type-II heterojunction photocatalyst, the CB and VB levels of semiconductor A are higher than the corresponding levels of semiconductor B [42-44]. Therefore, the photogenerated electrons will transfer to semiconductor B, while the photogenerated holes will migrate to semiconductor A under light irradiation, resulting in a spatial separation of electron-hole pairs. The redox ability of a type-II heterojunction photocatalyst will also be reduced due to the reduction reaction occurring on semiconductor B with a lower reduction potential and the oxidation reaction occurring on semiconductor A with a lower oxidation potential.The architecture of the type-III

heterojunction photocatalyst is similar to that of the type-II heterojunction photocatalyst, but the staggered gap becomes so extreme that the bandgaps do not overlap[45-46]. Therefore, electron-hole migration and separation between the two semiconductors cannot occur for the type-III heterojunction, making it unsuitable for enhancing the separation of electron-hole pairs. Among the conventional heterojunctions mentioned above, the type-II heterojunction is the most effective conventional heterojunction for improving photocatalytic activity due to its suitable structure for spatially separating electron-hole pairs. In the past several decades, extensive efforts have been made to prepare different type-II heterojunction photocatalysts, such as TiO_2/g-C_3N_4[47], $BiVO_4$/WO_3[48], g-C_3N_4–WO_3[49], and g-C_3N_4–$BiPO_4$[50], to enhance photocatalytic activity. Generally, type-II heterojunction photocatalysts exhibit good electron-hole separation efficiency, a wide light-absorption range, and fast mass transfer.

Zhou et al. developed a SnO_2/TiO_2 type-II heterojunction photocatalyst for RhB degradation through an electrophoretic-deposition (EPD) and calcination method [51]. Commercial TiO_2 was deposited onto F-doped SnO_2-coated glass using EPD and then calcined at various temperatures (200, 300, 400, 500, and 600 °C) to create crystallized SnO_2/TiO_2 type-II heterojunction photocatalyst films. All the samples showed good photocatalytic activity owing to the fast electron-hole separation through the type-II heterojunction between TiO_2 and SnO_2. The sample prepared at 400 °C exhibited the highest photocatalytic activity among all samples studied. This can be attributed to its optimal crystallinity and specific surface area, which reduce the number of recombination centers on the sample and provide a larger surface area with active sites for photocatalytic reactions. Ong et al. systematically explored the photocatalytic potential of two types of heterojunction photocatalysts, Type-I Ag/AgCl/g-C_3N_4 and Type-II Ag/AgBr/g-C_3N_4, with a focus on CO2 reduction [52]. Both Ag/AgCl/g-C_3N_4 and Ag/AgBr/g-C_3N_4 demonstrated effective photocatalytic performance in CO_2 reduction, particularly in CH4 production, attributed to the presence of the heterojunction, which improved the charge-carrier separation in these photocatalysts. Notably, Ag/AgBr/g-C_3N_4 exhibited significantly superior photocatalytic CO_2 reduction activity for CH_4 production compared with Ag/AgCl/g-C_3N_4. This difference was attributed to the formation of a type-II heterojunction in Ag/AgBr/g-C_3N_4, as opposed to the Type-I heterojunction in Ag/AgCl/g-C_3N_4. The type-II heterojunction facilitated the spatial separation of electrons and holes by accumulating them in the Ag/AgBr and g-C_3N_4 regions, respectively. This study conclusively demonstrated that type-II heterojunctions in photocatalysts are more effective than Type-I heterojunctions in enhancing their photocatalytic CO_2 reduction activity.

We have established a heterojunction between g-C_3N_4 and CoN_4. We extensively investigated the stability, transport, electronic, and optical properties of this heterojunction. Through the analysis of band edge potentials, we determined that the heterojunction can function as a photocatalyst for the water-splitting reaction. This was identified as a Type-I heterojunction. Because it operates as a Type-I heterojunction, the effective separation of electrons and holes is limited. Although g-C_3N_4/CoN_4 is a more efficient photocatalyst than g-C_3N_4 for water splitting, it does not exhibit good photocatalytic properties.

Enhancing the photocatalytic activity for water splitting in g-C_3N_4/CoN_4 requires adjusting the band energy alignment. Mechanical strain or an external electric field offers effective and practical means to tune the electronic properties of a 2D semiconductor and heterostructures[53-54]. Bai et al. explored the effective tuning of single-layer $ZnGeN_2$ to better align it with water redox potentials and enhance light absorption in the visible-light region under a tensile strain of 5% [55]. Edalati et al. proposed that under strain, $CsTaO_3$ and $LiTaO_3$ show optical bandgap narrowing, resulting in a 2.5-fold enhancement in photocatalytic hydrogen generation [56]. This finding aligns with Wang et al.'s discovery that biaxial strain effectively tunes the bandgap and band alignment of a 2D CdS/g-C_3N_4 heterostructure[57]. This tuning is crucial for visible-light photocatalytic water splitting, accelerating the separation of photogenerated carriers, and significantly improving the photocatalytic activity. Additionally, Dai et al. highlighted that ferroelectric photocatalysts could experience substantial improvements owing to the beneficial effects of the intrinsic internal electric field on the separation and migration of photogenerated carriers [58]. Exploring the potential of 2D ReS_2 for photocatalytic water splitting through strain and electric field functionalization, Pan et al. utilized first-principles calculations to demonstrate the significant impact of strain on the bandgap and band alignment of ReS_2[59]. The application of both tensile and compressive strains, whether axial or biaxial, results in a progressive reduction in the bandgap. This phenomenon is attributed to the strains inducing notable geometric distortion and causing charge rearrangement. While the band gap of ReS_2 remains unaffected by the electric field, the band alignment is highly influenced by it, as the electric field exerts minimal impact on the crystal structure but generates an in-plane dipole moment. Consequently, ReS_2 functionalized with a biaxial strain of 4% or an electronic field of -0.1 V A emerges as a promising candidate for a water-splitting photocatalyst. Chen et al explored the photocatalytic attributes of a ZnO monolayer under biaxial strain and an electric field [60]. This encompasses the investigation of parameters such as the bandgap, band edge position, and optical absorption spectra.

Remarkably, we identified that a ZnO monolayer subjected to 10% biaxial tensile strain exhibits promising characteristics as a water-splitting photocatalyst, attributable to its favorable bandgap, suitable band edge, and exceptional optical absorption. Concurrently, the oxidation capacity of the ZnO monolayer under 10% biaxial tensile strain increases, which is beneficial for enhancing the efficiency of the photocatalytic water splitting reaction. Rahimi et al investigated the modulation of electronic properties in the hg-C_3N_4/g-ZnO van der Waals (vdW) heterostructure through the application of either a perpendicular electric field or biaxial strain [61]. The objective was to achieve suitable bandgap type band alignment and transition for applications in photocatalytic water splitting. Initially, they demonstrated that the original hg-C_3N_4/g-ZnO heterostructure exhibited a Type-I indirect bandgap energy of 2.08 eV, with appropriate conduction band minimum (CBM) and valence band maximum (VBM) levels relative to the water-splitting reaction. Additionally, a substantial electrostatic potential difference of 11.18 eV was observed across the heterostructure, creating a sizable built-in electric field from hg-C_3N_4 to g-ZnO. This electric field facilitates the migration of photogenerated electrons in g-ZnO towards hg-C3N4, reducing the electron-hole recombination rate. Subsequently, Rahimi et al illustrated that by applying either a perpendicular electric field or biaxial strain, Type-I band alignment could be transformed into type-II or Z-scheme configurations deemed desirable for photocatalytic applications.

In this study, we employed density functional theory (DFT) calculations to investigate the electronic and optical characteristics of the van der Waals (vdW) heterostructure composed of heptazine-g-C_3N_4/CoN_4 under the influence of perpendicular electric fields and biaxial strain. Using an electric field of +0.5, +0.25, 0, -0.25 and -0.5 V/Å and biaxial strains of +6, +4, +2, 0, -6, -4, -2%, respectively, we found that g-C_3N_4/CoN_4 heterostructure transform from type-I to type-II photocatalyst for water splitting reaction. Additionally, our examination extended to explore the tuning of heterostructure properties, such as band alignment and the transition type of the bandgap, which decisively confirm its better photocatalytic activity as a type-II photocatalyst.

Computational Methods:

The spin-polarized density functional theory (DFT) implemented in Quantum Espresso simulation package was used for all structural and electronic properties calculations [62]. The exchange-correlation was accounted for by using the Perdew-Burke-Ernzerhof (PBE) functional in the Generalized Gradient Approximation (GGA) [63]. To address the

shortcomings of GGA in describing the partially filled d-orbital, we also employed the GGA+U method, which takes into account localized d-orbitals through coulomb and exchange corrections, while the s and p-orbitals are only accounted for by the GGA functional [64]. A value of 3.4 eV was used for Co atoms, as reported in several studies [64,65]. Ultrasoft pseudopotentials were used with a plane wave cutoff energy of 145 Ry for all systems, and a vacuum space of 30 Å was used to prevent spurious interactions in the non-periodic z-direction [66]. Initially, the bulk CoN_4 was considered, and the most stable (111) slab was created from the optimized primitive unit cell of CoN_4 using a k mesh of 8 x 8 x 1[67]. For the optimization of the g-C_3N_4 unit, a k mesh of 12 x 12 x 1 was used. Finally, 2 x 2 x 1 heptazine and √3 x √3 x 1 of CoN_4 (111) slab were used to form the heterojunction, which was found to have only a 3% lattice mismatch [68,69]. BURAI and VESTA were used for visualization and modeling purposes. All structural parameters were optimized using the Broyden, Fletcher, Goldfarb, Shanno (BFGS) algorithm and the dispersion-corrected GGA-PBE functional (Grimme-D2 scheme was used)[70]. The lattice parameters and atomic positions were optimized until all the forces were less than 10^{-3} Ry. After optimization, the charge density difference and work function calculations were performed on the heterostructure. The optical properties of the heterojunction, as well as the g-C_3N_4 and CoN_4 (111) slab, were calculated using the GGA-PBE method and the Cambridge Serial Total Energy Package (CASTEP) [71]. The band structure and related properties were calculated using the DFT+U method, and following several other studies, a Hubbard parameter Ueff=3.4 eV was used for the Co atom [64]. The DFT+U method accurately describes the strong on-site Coulomb repulsion of the localized Co 3d electrons using the following equation

$$E_{PBE+U} = E_{PBE} + \frac{U-J}{2}\sum_{\sigma} Tr[\rho^{\sigma}| - \rho^{\sigma}\rho^{\sigma}] \qquad (1)$$

Here, ρ^{σ} represents the spin-polarized on-site density matrix. The spherically averaged Hubbard parameter U characterizes the additional energy incurred from placing an extra electron at a given site, and the parameter J represents the screened exchange energy. However, during calculations, U and J are not considered independently; rather, their combined value, Ueff = U - J, is considered as necessary and meaningful because it accounts for the on-site Coulomb repulsion on each affected orbital.

The work function provides information about the relative position of the Fermi level and evaluates the band alignment at the interface and therefore is a significant electronic property

of photocatalytic materials. The work function represents the energy required to extract an electron from the Fermi surface of a solid to a vacuum at absolute zero and represented by the following formula [72]

$$\phi = E_{vacuum} - E_{fermi} \quad (2)$$

Here, E_{fermi} and E_{vacuum} represent the energy of a stationary electron at the Fermi level and in the vacuum adjacent to the surface.

We have calculated the optical properties of the systems under strain and electric field. Optical absorption spectrum reflects the solar energy absorption rate of photo catalyst.

The absorption spectra can be calculated by the equation [73]

$$I(\omega) = [\sqrt{2}\omega\sqrt{(\varepsilon(\omega)_1^2 + (\varepsilon(\omega)_2^2} - \varepsilon(\omega)_1]^{1/2} \quad (3)$$

$\varepsilon(\omega)_1$ is the real part and $\varepsilon(\omega)_2$ is the imaginary part of the dielectric function.

We have calculated the optical band gap of g-C_3N_4 and heterojunctions using Tauc method [74]

$$(\alpha h\nu)^m = A_0\left(h\nu - E_g^{opt}\right) \quad (4)$$

α : absorption coefficient,

hν : the incident photon energy

E_g^{opt} : optical band gap

A_0 is a constant depending on the transition probability.

The relationship that relates the wavelength of light (λ) to the optical band gap energy (Eg) in a material. This relationship is commonly expressed by the equation:

$$\lambda = \frac{1240}{E_g} \quad (5)$$

Here,

λ is the wavelength of light in nanometers (nm).

E_g is the optical band gap.

The constant 1240 is a conversion factor that relates energy in electron volts to wavelength in nanometers.

Results and Discussions:

Geometry Structures and Thermodynamic Stability

In this study, we explore the geometric structures and thermodynamic stability of pure bulk g-C_3N_4. Four different connection patterns are known for g-C_3N_4: (a) monoclinic heptazine-based structure, (b) hexagonal heptazine-based structure, (c) orthorhombic triazine-based structure, and (d) hexagonal triazine-based structure [75]. Previous studies indicate that the hexagonal heptazine-based g-C_3N_4 is the most stable among these patterns [75]. Consequently, we focus exclusively on the energetically most stable graphitic phase for our investigation.

The single-layered g-C_3N_4 sheet is obtained by cleaving the surface of the optimized bulk structure. We begin by considering this single-layered structure to comprehend its geometrical and electronic characteristics. Heptazine g-C_3N_4 comprises heptazine (C_6N_7) units arranged in a 2D lattice, connected via C-N bonds to form a hexagonal network (see Fig.1(a)). The unit cell of the hexagonal lattice consists of 14 atoms (8N + 6C), with two types of C atoms and three types of N atoms [76]. The optimization of the g-C3N4 unit cell is performed using ultrasoft pseudopotentials with a k mesh of 12 12 1 and a cutoff energy of 145 Ry. The optimized unit cell geometry is presented in Fig.1(a), and the lattice parameters are tabulated in Table 1, showing good agreement with experimental and theoretical values.

Moving on to the CoN_4 structure, we consider the same diamond-like crystal structure of bulk CoN_4, relax it using the conventional GGA-PBE functional, and create the primitive unit cell geometry of CoN_4 from the optimized bulk structure [65]. The calculated formation energy and total energies of different magnetic states confirm the stability of the CoN_4 structure, with the ferromagnetic state being the most stable. The lattice parameters and bond lengths of CoN_4 are consistent with reported values [65].

To create a realistic model system for the g-C_3N_4 and CoN_4 heterojunction, we initiated the study by calculating the surface energy (γ) of the (100), (110), and (111) CoN_4 slabs using the formula

$$\gamma = \frac{E_{slab} - E_{bulk}}{2A} \qquad (6)$$

Here $E_{(slab)}$ and $E_{(bulk)}$ are denoting the energies of the slab and bulk CoN_4. A is the area of the slab. The CoN4 slab was constructed by cleaving the primitive unit cell into (100), (010), and (001) planes, with atomic layers separated by a vacuum space of 30 Å. The resulting surface energies for the (100), (110), and (111) CoN_4 slabs were determined to be 0.36, 0.37, and 0.11 J/m², respectively, as presented in Table 1. The (111) CoN_4 slab, being the most stable, was selected for heterojunction formation and subsequent calculations.

Table 1 - Calculated energies of the systems and surface energies of slabs.

System	g-C_3N_4 (2× 2×1)	CoN_4 bulk	CoN_4(111) slab ($\sqrt{3} \times \sqrt{3} \times 1$)	g-C_3N_4/CoN_4
Energy(Ry)	-951.88	-2987.11	-2240.15	-3192.38
Surface energy(J/m^2)		(100) (110) (111)		
		0.36 0.37 0.11		

Consistent with prior studies, we ensured lattice compatibility in the interface model system by aligning a 2×2×1 heptazine with $\sqrt{3} \times \sqrt{3} \times 1$ of CoN_4 (111) slab

The calculated lattice mismatch (δ) was approximately 3%, within a reasonable and acceptable range [69,77]. The lattice mismatch was determined using the equation:

$$\delta = \frac{a(111) - a(g)}{a(111)} \qquad (7)$$

Here a (111) and a(g) represent the relaxed lattice parameters of CoN_4 (111) and g-C_3N_4 monolayer, respectively. The constructed heterojunction model consists of 86 atoms (56 belonging to g-C_3N_4 and 30 to CoN_4 (111)), with the optimized geometry showing a stable interface with a distance of 2.0 Å between g-C_3N_4 and CoN4 (111) units. The optimized geometry of the interface is depicted in Fig.1(c) and Fig.1(d).

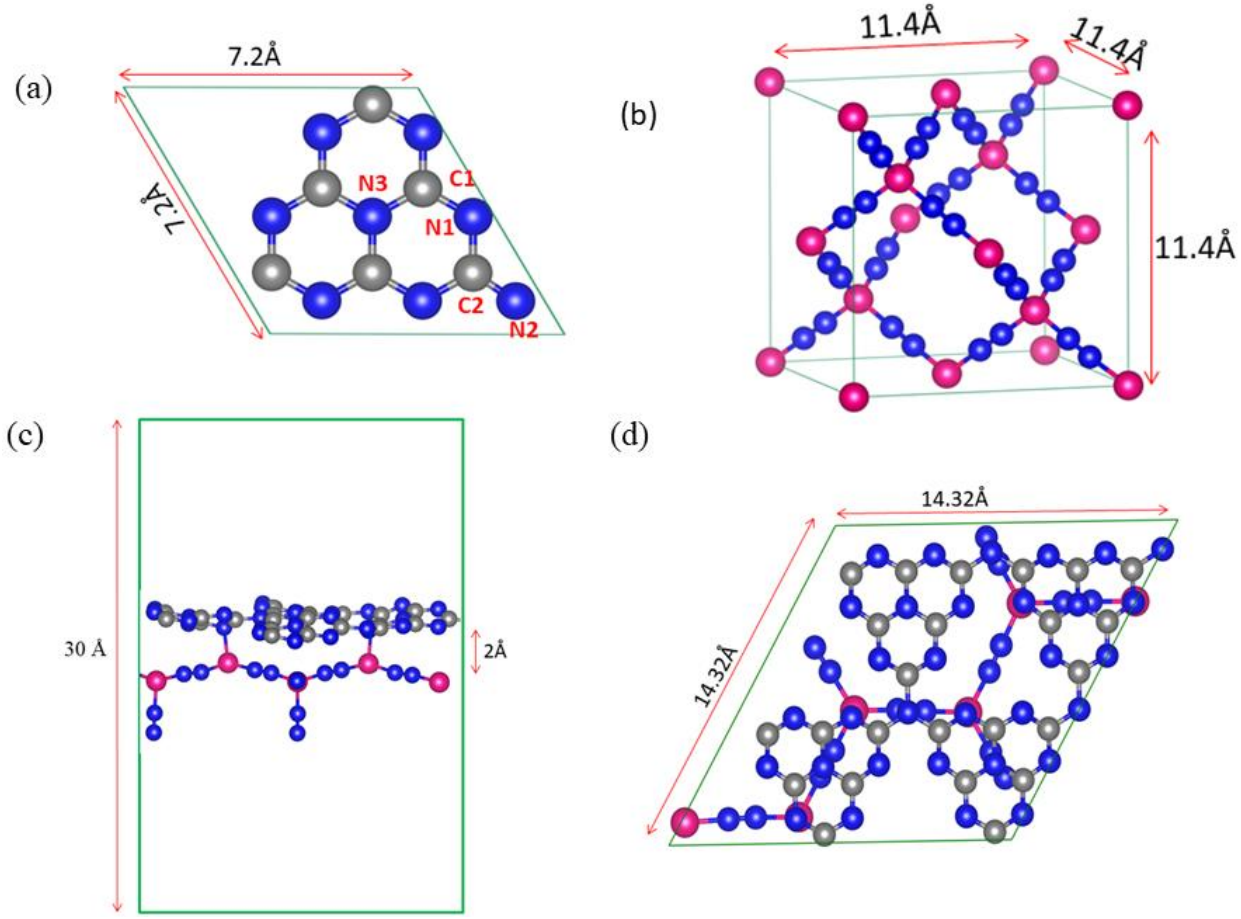

Fig.1-Optimized geometric structures of (a) g-C_3N_4 primitive unit cell (b) CoN_4 bulk (c) g-C_3N_4/CoN_4 heterojunction (side view) and (d) g-C_3N_4/CoN_4 heterojunction (top view).

Table 2- Lattice parameters for isolated systems (g-C_3N_4 and CoN_4) and heterojunction g-C_3N_4/CoN_4

System	Calculated lattice parameters(Å)			Reported lattice parameters(Å)		
	a	b	c	a	b	c
g-C_3N_4	7.20	7.20	-	7.2* 7.14**	7.2* 7.14**	-
CoN_4	11.4	11.4	11.4	11.23***	11.23***	11.23***
CoN_4(111) slab	8.06	8.06	30	-	-	-
g-C_3N_4/CoN_4	14.32	14.32	30	-	-	-

* A.M. Silva, M.I. Rojas,Computational and Theoretical Chemistry 1098 (2016) 41–49

**Jianjun Liu, Enda Hua,J. Phys. Chem. C 2017, 121, 25827-25835

***Jun Deng, Ning Liu, Jiangang Guo, Xiaolong Chen, PHYSICAL REVIEW B 99, 184409 (2019)

To understand the thermodynamic stability of the heterojunction as well as the interaction between g-C_3N_4 and CoN_4(111), the adhesion energy was calculated using equation (8) [78].

$$E_{ad} = E_{gC_3N_4/CoN_4} - E_{gC_3N_4} - E_{CoN_4} \qquad (8)$$

$E_{gC_3N_4/CoN_4}$, $E_{gC_3N_4}$ and E_{CoN_4} represent the total energies of the relaxed g-C_3N_4/CoN_4 heterostructure, g-C_3N_4 monolayer and CoN_4(111) slab. The interface E_{ad} was calculated as -4.7396 eV. The negative adhesion energy of the heterojunction indicates that the adsorption is thermodynamically stable [79]. This furthermore confirms that the process of adhesion of CoN_4 on the g-C_3N_4 surface is exothermic and energetically favourable [79]

Effect of biaxial strain

To investigate the modulation of electronic and optical properties in the g-C_3N_4/CoN_4 heterojunction for enhanced photocatalytic efficiency, we introduced biaxial strain within a range spanning from -6% (compressive) to +6% (tensile). We calculated the percent applied biaxial strain according to[60]

$$\%\ strain = \frac{a-a_0}{a} \times 100 \qquad (9)$$

where a and a_0 are the lattice constants of the g-C_3N_4/CoN_4 before and after the applied biaxial strain

The structural relaxation along the z-axis was permitted while keeping the cell dimensions fixed. The schematic representation of application of strain is shown in Fig.2. Green arrows represent tensile strain and red colour arrows represent compressive strain.

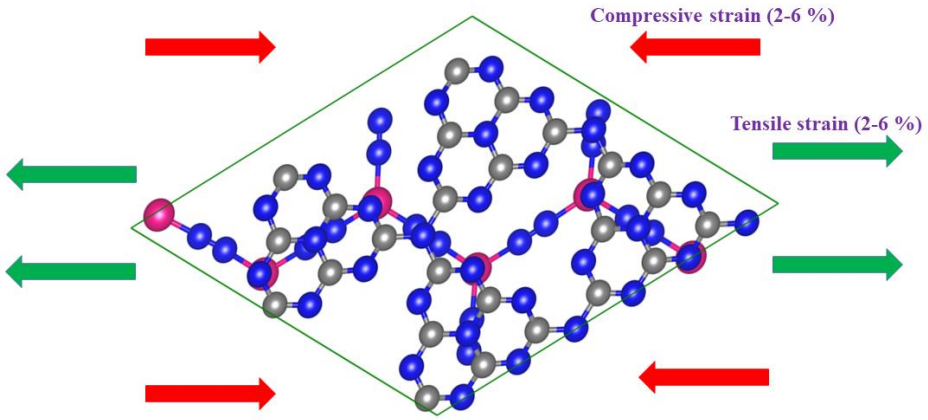

Fig.2-Schematic illustration of tensile and compressive biaxial strain on g-C_3N_4/CoN_4 heterojunction

The application of significant compressive strains, such as the -6% compressive strain, poses experimental challenges, necessitating extremely high pressures. Nonetheless, for comprehensive exploration, we extended the study until the elimination of the semiconducting behaviour in the heterojunction was observed, particularly at the -6% compressive strain.

The atomic positions in a relaxed state are presented in Table 3. Tensile strains had a minimal impact on the interlayer distance but led to a reduction in buckling in both layers. There is a remarkable increase in the buckling of g-C_3N_4 observed at +6% strain. Nevertheless, compressive strains significantly influenced the structure. As compressive strain increased, the interlayer distance decreased, but the buckling of both monolayers increased. This suggests that the heterostructures can withstand a range of strains, except for substantial compressive strains.

Table 3- Influence of biaxial strain on the structure of the g-C_3N_4/CoN_4 heterostructure

Strain [%]	Heterostructure interlayer distance [Å]	Buckling in hg-C3N4 [Å]
-6	1.97	2.91
-4	1.93	2.34
-2	2	1.56
0	2.05	1.2
+2	2.03	0.76
+4	2.05	0.7
+6	2.05	3.6

Electronic properties

Via biaxial strain, the band gap underwent tuning. Shown in Fig. 3 is the schematic illustrating the adjustment of the band gap through biaxial strain. The variation of biaxial strain ranges from -6% to +6% in increments of 2%, where positive values represent tensile strains, and negative values signify compressive strains. In Fig. 3, it is evident that both tensile and compressive strains contribute to the reduction of the band gap. In the range from -6% to +4% strain, the systems exhibit half-metallic characteristics. This implies that one spin channel demonstrates semiconducting behaviour, while the other spin channel exhibits metallic behaviour. However, at +6% strain, the system transitions to metallic behaviour entirely. In this state, one spin channel registers 0.98 eV, while the other spin channel displays 0.27 eV. In the non-strained system, the highest band gap is observed, with the spin-up channel exhibiting a 1.81 eV band gap, while the spin-down channel displays a zero band gap.

As depicted in the Fig.3, the bandgap transition type remains unaltered (direct) under tensile (positive) strains. Conversely, compressive(negative) strain induces a band gap transition. Specifically, as the strain increases from +2% to +6%, the direct band gap transforms into an indirect band gap. Upon exposure to solar irradiation on the surface of the g-C_3N_4/CoN_4 monolayer, electrons in the valence band undergo direct transitions to the conduction band, a process facilitated more easily than an indirect transition. Tensile(positive) and compressive(negative) strains transform the type 1 heterojunction into a type 2 heterojunction.

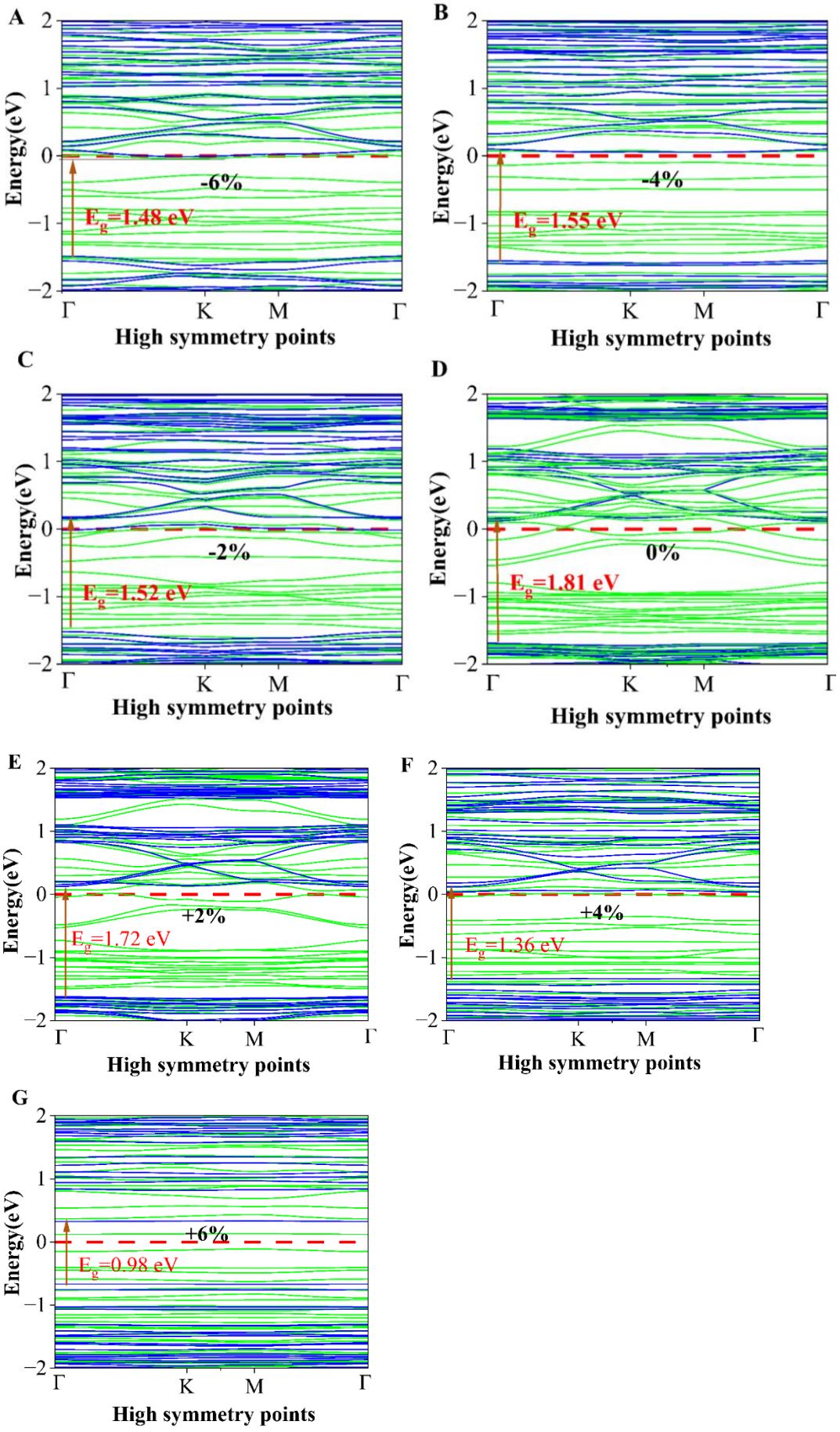

Fig.3-Electronic band structures of the g-C_3N_4/CoN_4 heterojunction under biaxial strain

Optical properties

Optical absorption spectrum reflects the solar energy absorption rate of photo catalyst. To investigate the effect of strain on the optical absorption of g-C_3N_4/CoN_4, the visible light absorption spectra of g-C_3N_4/CoN_4 heterojunction under different strains are plotted in Fig.4. In the range from 1.5 eV to 3.5 eV, the optical absorption is enhanced under both 2% tensile and 2% compressive strains compared to the non-strained system.

To analyse the absorption maxima we have also calculated optical band gap by tauc method, which is shown in equation (4). The optical band gaps of strained systems given in table 4. Systems with +2% tensile strain, -2% compressive strain, and non-strained conditions act as effective photocatalysts due to their absorption maxima occurring at longer wavelengths.

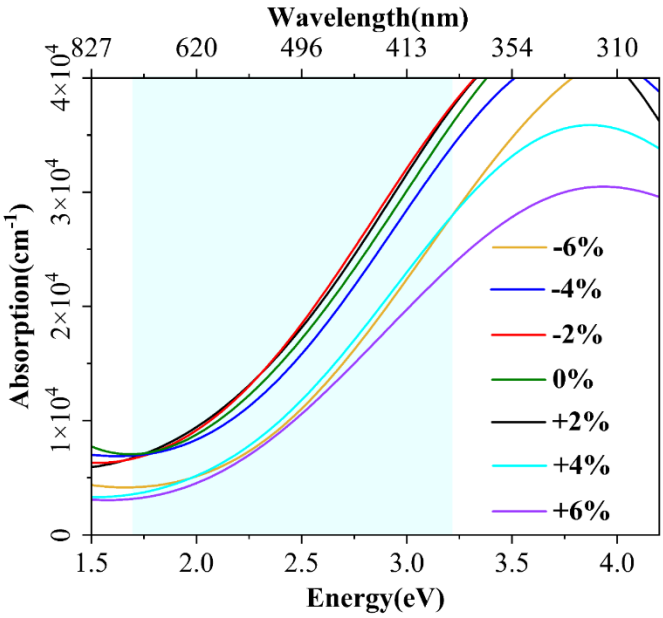

Fig.4-Optical absorption spectra of the g-C_3N_4/CoN_4 heterojunction under biaxial strain

Photocatalytic water splitting

The determination of the strength of the redox reaction and the potential application of the g-C_3N_4/CoN_4 heterostructure for water splitting relies on the accurate detection of band alignment. Ideally, for efficient water splitting, the VBM band position should be higher than the O_2/H_2O potential (0 V vs. NHE), and the CBM band position should be lower than the H^+/H_2 potential (1.23 V vs NHE). However, due to the inherent challenge of obtaining the

VBM and CBM on an absolute scale using DFT, this study examines the band-edge positions of the heterojunction relative to the Normal Hydrogen Electrode. The positions of the vacuum level were set at zero, and the VBM and CBM positions were determined with respect to the vacuum level using the GGA+U method. The band-edge potentials of the proposed system are illustrated in Fig. 5. The calculated O_2/H_2O reduction potential with respect to vacuum energy is -4.5 eV, and the H+/H2 oxidation potential with respect to vacuum energy is -5.73 eV. We have analysed the band-edge potentials of the systems. Tensile-strained systems at +4% and +6% cannot be utilized for water splitting reactions. However, all other systems are suitable for water splitting reactions.

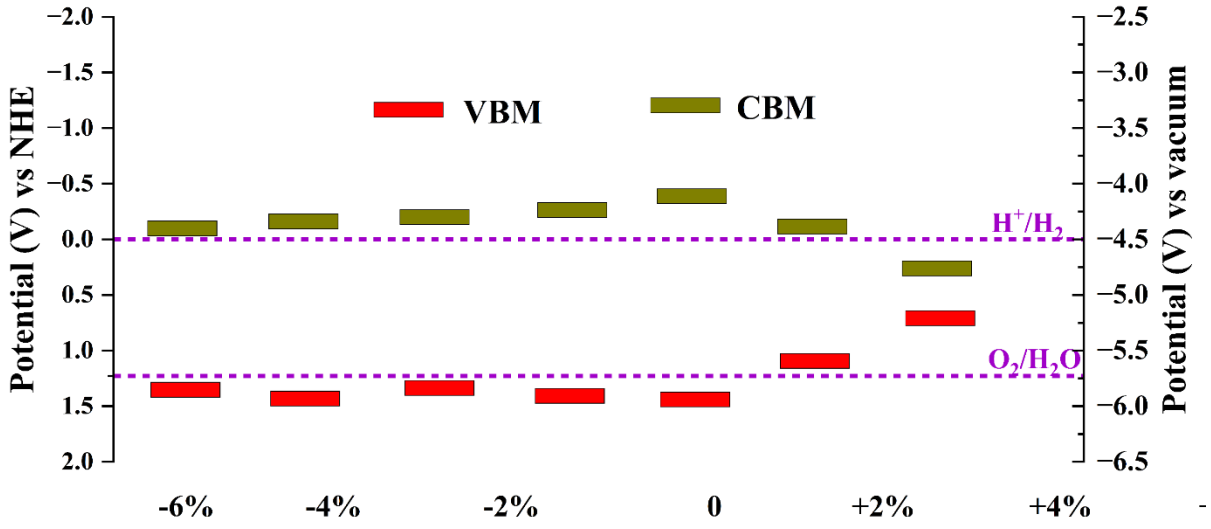

Fig.5- Effect of the biaxial strain on the band edge position of the g-C_3N_4/CoN_4 heterojunction

Table 4- Influence of biaxial strain on the electronic and optical properties g-C_3N_4/CoN_4 heterostructure

Strain	Optical band gap (eV)	Electronic band gap(eV)	Type of heterojunction	Possibility of water splitting	Direct or indirect band gap
+6	2.43	0.98 spin up 0.27 spin down	Type 11	Not possible	Direct
+4	2.42	1.36	Type 11	Not possible	Direct
+2	2.1	1.72	Type 1	possible	Direct
0	2.0	1.8 1	Type 1	possible	Direct
-2(good photocatalyst)	2.1	1.52	Type 11	possible	Direct
-4	2.3	1.55	Type 11	possible	Direct
-6	2.4	1.48	Type 11	possible	Indirect

Improving photocatalytic performance with band gap tuning via external electric field

In our effort to adjust the band gap of g-C3N4/CoN4, we varied the external electric field. As illustrated in Fig.6, the electric field was applied along the Z-axis direction. The external electric field was systematically altered, ranging from -0.5 V/Å to 0.5 V/Å in increments of 0.25 V/Å.

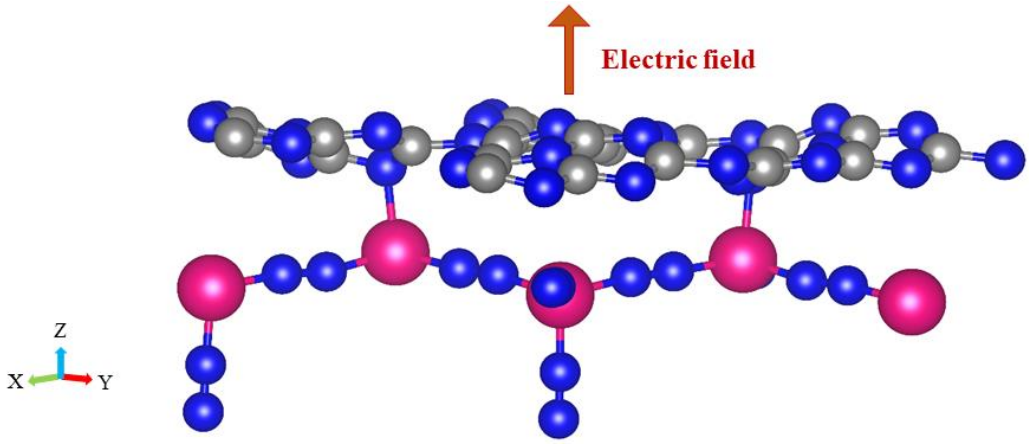

Fig.6-Schematic illustration of tensile and compressive biaxial strain on g-C_3N_4/CoN_4 heterojunction

Electronic properties

When applying the electric field in both directions, the band gap decreases. However, the nature of the band gap does not change with an electric field; all band gaps remain direct band gaps at the Γ position. The heterojunction's nature changes when an electric field is applied. Specifically, a type 1 heterojunction transforms into a type 2 heterojunction under

the influence of an electric field.

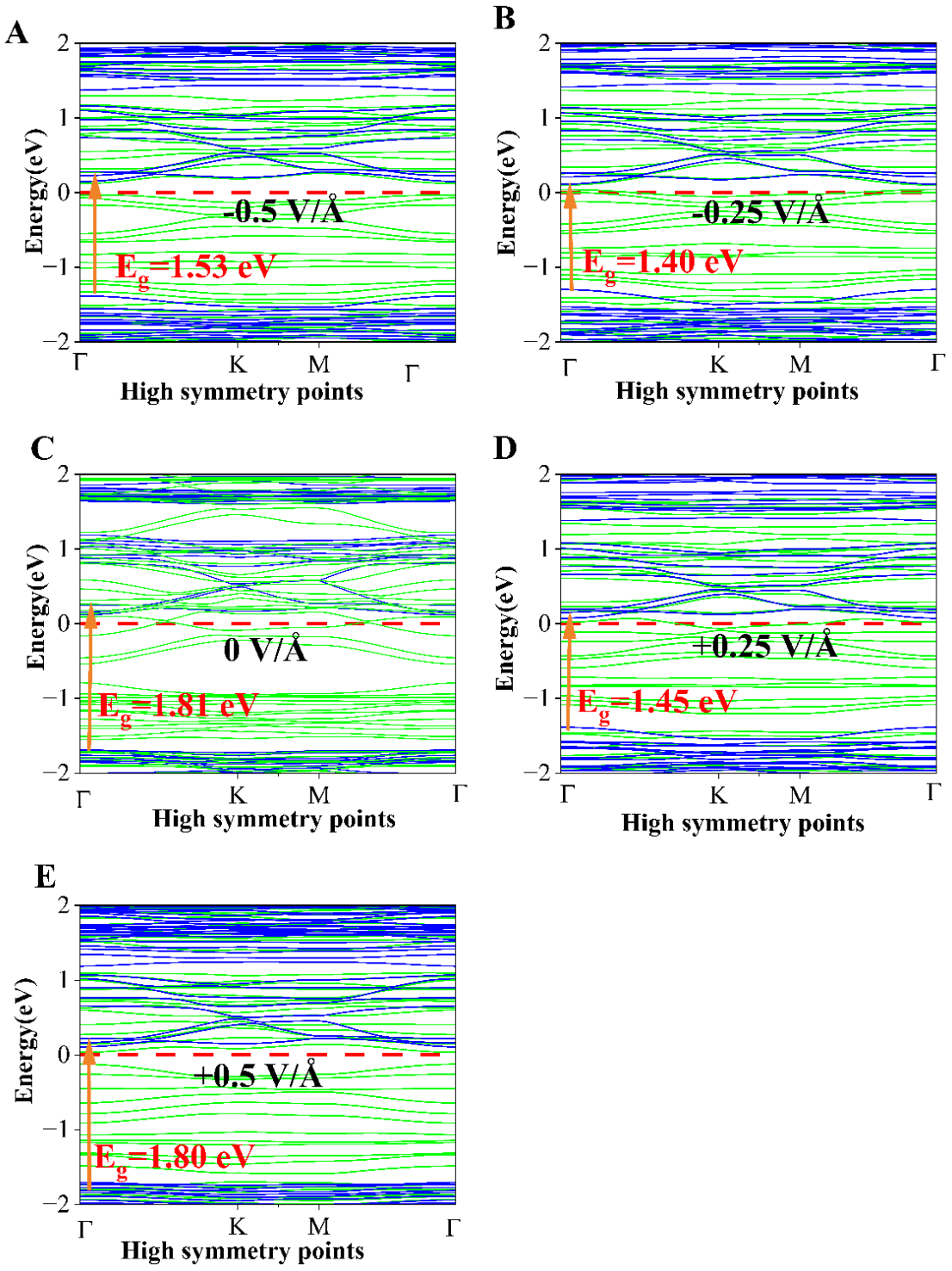

Fig.3-Electronic band structures of the g-C_3N_4/CoN_4 heterojunction under electric field

Optical properties

We did not observe a significant change in the optical properties of the system when applying an electric field. However, a slight enhancement in optical absorption, ranging from 1.75 eV

to 2.5 eV, was observed when applying electric fields of 0.5 V/Å and -0.5 V/Å.

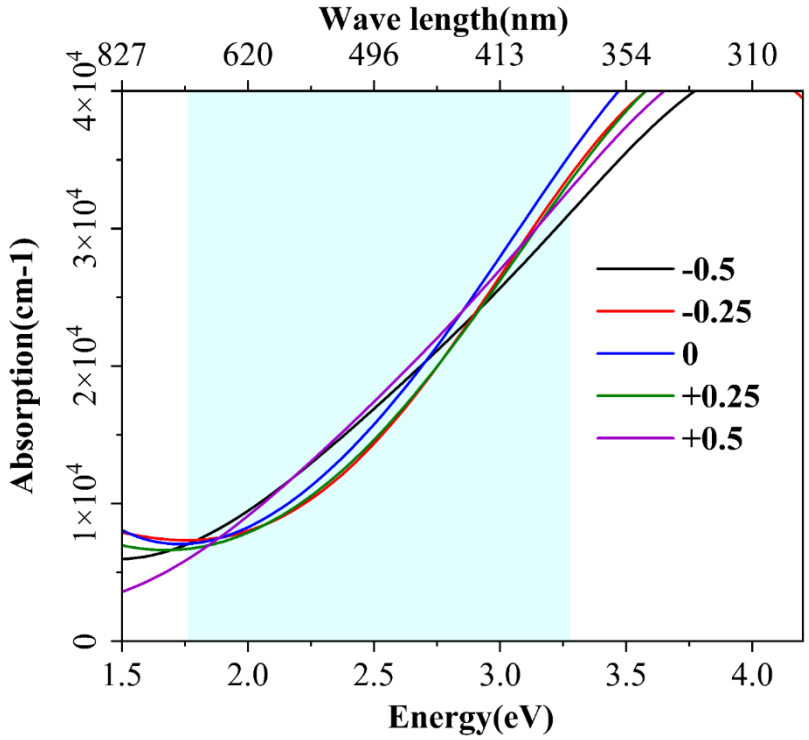

Fig.8-Optical absorption spectra of the g-C_3N_4/CoN_4 heterojunction under biaxial electric field

Possibility of water splitting

We have analysed the band-edge potentials of the systems. Systems subjected to an electric field at 0.25 V/Å and -0.25 V/Å cannot be utilized for water-splitting reactions. However, all other systems are suitable for water-splitting reactions.

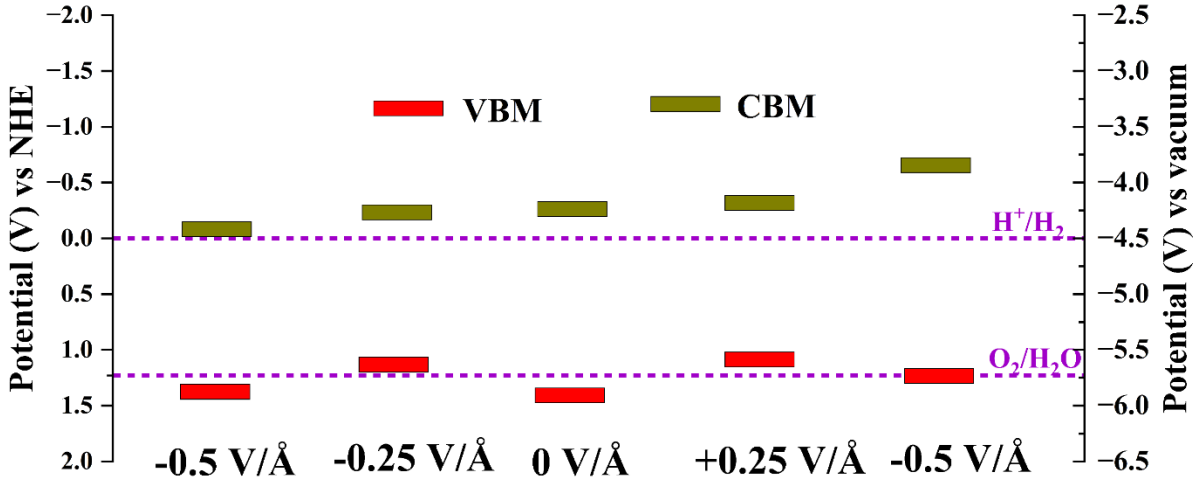

Fig.9- Effect of the biaxial strain on the band edge position of the g-C_3N_4/CoN_4 heterojunction

Table 4- Influence of electric field on the electronic and optical properties g-C_3N_4/CoN_4 heterostructure

Electric field (V/Å)	Optical band gap(eV)	Electronic band gap(eV)	Type of heterojunction	Possibility of water splitting	Direct or indirect band gap
-0.5	1.88	1.53	Type 11	possible	Direct
-0.25	1.9	1.4	Type 11	Not possible	Direct
0	2	1.81	Type 1	possible	Direct
+0.25	1.94	1.45	Type 11	Not possible	Direct
+0.5	1.9	1.8	Type 11	possible	Direct

Mechanism of photocatalytic water splitting

Commonly, there are three categories of traditional heterojunction photocatalysts: those exhibiting a straggling gap (Type-I), those featuring a staggered gap (Type-II), and those with a broken gap (Type-III) [40]. In the case of a Type-I heterojunction photocatalyst, semiconductor A's conduction band (CB) and valence band (VB) are higher and lower, respectively, than those of semiconductor B [41]. Consequently, when exposed to light, electrons and holes accumulate at the CB and VB levels of semiconductor B, respectively. However, since both electron-hole pairs accumulate within the same semiconductor, effective separation is hindered for the Type-I heterojunction photocatalyst. Moreover, a redox reaction takes place on the semiconductor with the lower redox potential, significantly diminishing the heterojunction photocatalyst's redox capability.

On the contrary, for the Type-II heterojunction photocatalyst, semiconductor A's CB and VB levels are higher than those of semiconductor B [42-44]. Consequently, photogenerated electrons migrate to semiconductor B, while photogenerated holes move to semiconductor A under light irradiation, leading to spatial separation of electron-hole pairs. The redox ability of a Type-II heterojunction photocatalyst is also diminished due to the reduction reaction occurring on semiconductor B with a lower reduction potential and the oxidation reaction taking place on semiconductor A with a lower oxidation potential.

The architecture of the Type-III heterojunction photocatalyst is akin to that of the Type-II heterojunction photocatalyst, but the staggered gap is so extreme that the bandgaps do not overlap [45-46]. Consequently, electron-hole migration and separation between the two semiconductors are impeded for the Type-III heterojunction, rendering it unsuitable for

enhancing the separation of electron-hole pairs. Among the mentioned conventional heterojunctions, the Type-II heterojunction stands out as the most effective for improving photocatalytic activity due to its structure conducive to spatially separating electron-hole pairs. Tensile(positive), compressive(negative) strains and external electric field transform the type 1 heterojunction into a type 2 heterojunction. On applying strain and electric field the photocatalytic activity of the heterojunction increases.

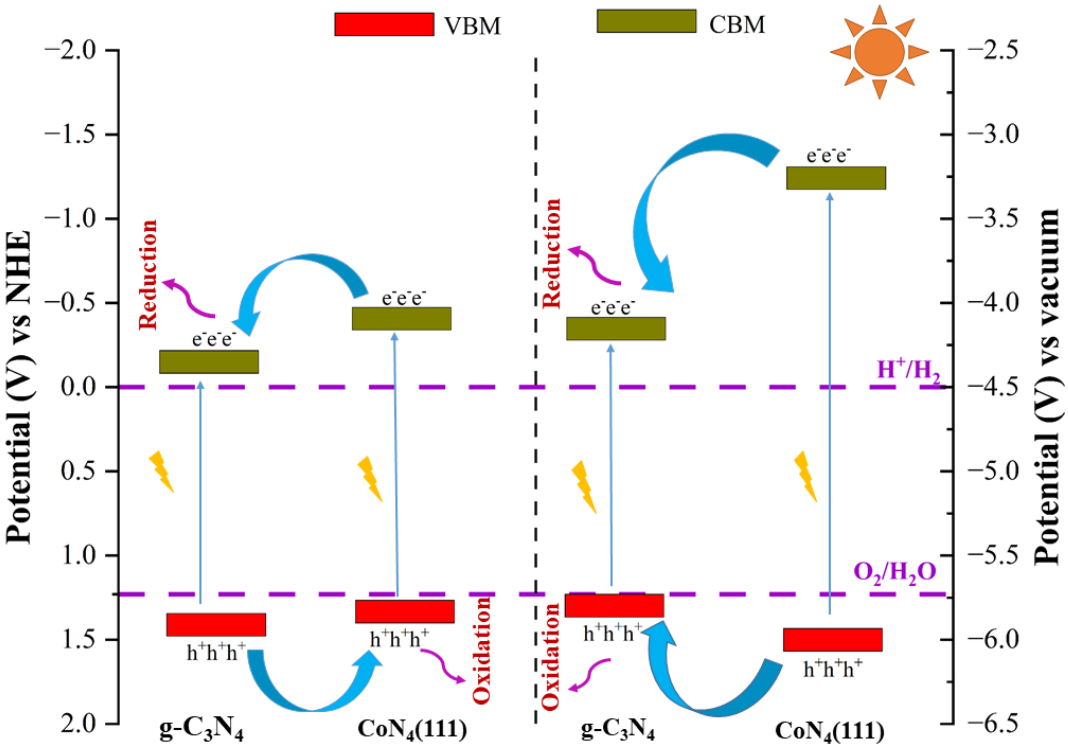

Fig.10- Band edge positions and possible mechanism of water splitting of heterojunction under a compressive strain of 2% and Original heterojunction

Conclusion

Van der Waals (vdW) heterojunctions, composed of two-dimensional monolayers, represent a recent class of materials known for their highly adaptable band alignment, bandgap energy, and bandgap transition characteristics. In this study, we utilized density functional theory calculations to investigate the formation of a vdW heterojunction involving a monolayer of heptazine-based graphitic carbon nitride (g-C_3N_4) and a CoN_4 (111) slab, denoted as g-C_3N_4/CoN_4. This particular heterojunction shows potential as a catalyst for solar-driven photocatalysis in the water-splitting reaction.

Upon the establishment of the heterojunction, a type-I direct bandgap (Eg = 2.00 eV) is achieved, featuring appropriate conduction band minimum and valence band maximum levels in relation to the oxidation/reduction potentials for the water-splitting reaction. Furthermore, the band alignment, bandgap energy, and transition type of the heterojunction can be adjusted by applying external perpendicular electric fields and biaxial strains. Notably, a -2% strain

induces a type-II band alignment (Eg = 2.1 eV, direct), while an electric field of 0.5 V/Å also leads to a type-II heterostructure (Eg = 1.90 eV, direct). Both configurations demonstrate advantages for efficient water-splitting photocatalysis.

Acknowledgments

M. Chattopadhyaya acknowledges the SERB POWER GRANT. Dhilshada V N acknowledges the UGC for providing the fellowship grant. The author M. Chattopadhyaya also acknowledge the center for Computational Modeling and Simulation (CCMS), NIT Calicut, for computational support.

References

1. Grubler, A.; Wilson, C.; Bento, N.; Boza-Kiss, B.; Krey, V.; McCollum, D. L.; Rao, N. D.; Riahi, K.; Rogelj, J.; De Stercke, S.; Cullen, J.; Frank, S.; Fricko, O.; Guo, F.; Gidden, M.; Havlík, P.; Huppmann, D.; Kiesewetter, G.; Rafaj, P.; Schoepp, W.; Valin, H. A Low Energy Demand Scenario for Meeting the 1.5 °C Target and Sustainable Development Goals without Negative Emission Technologies. *Nat. Energy* **2018**, *3* (6), 515–527. DOI: 10.1038/s41560-018-0172-6
2. Li, C.; Liu, X.; Yan, Y.; Song, X.; Yan, Y.; Liu, C.; Xu, R.; Huo, P. Synergy between Cu Doping and Catalytic Platform in 2D Ni-MOFs/Cu-Zn0.5Cd0.5S for Efficient Water-To-Hydrogen Conversion. *Chem. Eng. J.* **2021**, *410*, 128316. DOI: 10.1016/j.cej.2020.128316
3. Huang, W.-Y.; Shen, Z.-Q.; Cheng, J.-Z.; Liu, L.-L.; Yang, K.; Chen, X.; Wen, H.-R.; Liu, S.-Y. C–H Activation Derived CPPs for Photocatalytic Hydrogen Production Excellently Accelerated by a DMF cosolvent. *J. Mater. Chem. A* **2019**, *7* (42), 24222–24230. DOI: 10.1039/C9TA06444C
4. Cheng, J.-Z.; Liu, L.-L.; Liao, G.; Shen, Z.-Q.; Tan, Z.-R.; Xing, Y.-Q.; Li, X.-X.; Yang, K.; Chen, L.; Liu, S.-Y. Achieving an Unprecedented Hydrogen Evolution Rate by Solvent-Exfoliated CPP-

Based Photocatalysts. *J. Mater. Chem. A* **2020**, *8* (12), 5890–5899. DOI: 10.1039/C9TA13514F

5. Wu, Q.; Wang, J.; Wang, Z.; Xu, Y.; Xing, Z.; Zhang, X.; Guan, Y.; Liao, G.; Li, X. High-Loaded Single Cu Atoms Decorated on N-Doped Graphene for Boosting Fenton-Like Catalysis Under Neutral pH. *J. Mater. Chem. A* **2020**, *8* (27), 13685–13693. DOI: 10.1039/D0TA04943C
6. Li, C.; Che, H.; Yan, Y.; Liu, C.; Dong, H. Z-Scheme AgVO3/ZnIn2S4 Photocatalysts: "One Stone and Two Birds" Strategy to Solve Photocorrosion and Improve the Photocatalytic Activity and Stability. *Chem. Eng. J.* **2020**, *398*, 125523. DOI: 10.1016/j.cej.2020.125523
7. Xiong, H.; Wu, L.; Liu, Y.; Gao, T.; Li, K.; Long, Y.; Zhang, R.; Zhang, L.; Qiao, Z.-A.; Huo, Q.; Ge, X.; Song, S.; Zhang, H. Controllable Synthesis of Mesoporous TiO 2 Polymorphs with Tunable Crystal Structure for Enhanced Photocatalytic H 2 Production. *Adv. Energy Mater.* **2019**, *9* (31), 1901634. DOI: 10.1002/aenm.201901634
8. Dai, C.; Liu, B. Conjugated Polymers for Visible-Light-Driven Photocatalysis. *Energy Environ. Sci.* **2020**, *13* (1), 24–52. DOI: 10.1039/C9EE01935A
9. Oka, K.; Nishide, H.; Winther-Jensen, B. Completely Solar-Driven Photoelectrochemical Water Splitting Using a Neat Polythiophene Film. Cell Rep. *Physiol. Sci.* **2021**, *2*, 100306.
10. Yang, L.; Fang, N.; Wang, Q.; Chu, Y.; Xu, J.; Deng, F. Surface Water Loading on Titanium Dioxide Modulates Photocatalytic Water Splitting. Cell Rep. *Physiol. Sci.* **2020**, *1*, 100013.
11. Guo, T.; Wang, K.; Zhang, G.; Wu, X. A Novel α-Fe2O3@g-C3N4 Catalyst: Synthesis Derived from Fe-Based MOF and Its Superior Photo-Fenton Performance. *Appl. Surf. Sci.* **2019**, *469*, 331–339. DOI: 10.1016/j.apsusc.2018.10.183
12. Liao, G.; Zhong, L.; Cheung, C. S.; Du, C.; Wu, J.; Du, W.; Zheng, H.; Gao, H. Direct Synthesis of Hypercrosslinked Microporous Poly(Para-Methoxystyrene) for Removal of Iron(III) Ion from Aqueous Solution. *Micropor. Mesopor. Mater.* **2020**, *307*, 110469. DOI: 10.1016/j.micromeso.2020.110469
13. Liao, G.; Fang, J.; Li, Q.; Li, S.; Xu, Z.; Fang, B. Ag-Based Nanocomposites: Synthesis and Applications in Catalysis. *Nanoscale* **2019**, *11* (15), 7062–7096. DOI: 10.1039/c9nr01408j

14. Dhakshinamoorthy, A.; Li, Z.; Garcia, H. Catalysis and Photocatalysis by Metal Organic Frameworks. *Chem. Soc. Rev.* **2018**, *47* (22), 8134–8172. DOI: 10.1039/c8cs00256h

15. Xu, H.; She, X.; Fei, T.; Song, Y.; Liu, D.; Li, H.; Yang, X.; Yang, J.; Li, H.; Song, L.; Ajayan, P. M.; Wu, J. Metal-Oxide-Mediated Subtractive Manufacturing of Two-Dimensional Carbon Nitride for High-Efficiency and High-Yield Photocatalytic H2 Evolution. *A.C.S. Nano* **2019**, *13* (10), 11294–11302. DOI: 10.1021/acsnano.9b04443

16. Ding, G.; Wang, Q.; Liu, F.; Dan, Y.; Jiang, L. A Novel Iron-Chelating Polyimide Network as a Visible-Light-Driven Catalyst for Photoinduced Radical Polymerization. *Chin. J. Catal.* **2021**, *42* (1), 141–151. DOI: 10.1016/S1872-2067(20)63610-5

17. Yan, C.; Barlow, S.; Wang, Z.; Yan, H.; Jen, A. K.-Y.; Marder, S. R.; Zhan, X. Non-Fullerene Acceptors for Organic Solar Cells. *Nat. Rev. Mater.* **2018**, *3* (3), 18003. DOI: 10.1038/natrevmats.2018.3

18. Volokh, M.; Peng, G.; Barrio, J.; Shalom, M. Carbon Nitride Materials for Water Splitting Photoelectrochemical Cells. *Angew. Chem. Int. Ed. Engl.* **2019**, *58* (19), 6138–6151. DOI: 10.1002/anie.201806514

19. Wang, K.; Hou, Y.; Poudel, B.; Yang, D.; Jiang, Y.; Kang, M.-G.; Wang, K.; Wu, C.; Priya, S. Melanin–Perovskite Composites for Photothermal Conversion. *Adv. Energy Mater.* **2019**, *9* (37), 1901753. DOI: 10.1002/aenm.201901753

20. Chen, S.; Takata, T.; Domen, K. Particulate Photocatalysts for Overall Water Splitting. *Nat. Rev. Mater.* **2017**, *2* (10), 17050. DOI: 10.1038/natrevmats.2017.50

21. Kumaravel, V.; Mathew, S.; Bartlett, J.; Pillai, S. C. Photocatalytic Hydrogen Production Using Metal Doped TiO2: A Review of Recent Advances. *Appl. Catal. B* **2019**, *244*, 1021–1064. DOI: 10.1016/j.apcatb.2018.11.080

22. Lei, G.; Dai, Z.; Fan, Z.; Zheng, X.; Cao, Y.; Shen, L.; Xiao, Y.; Au, C.; Jiang, L. Porous Nanosheets of Carbon-Conjugated Graphitic Carbon Nitride for the Oxidation of H2S to Elemental Sulfur. *Carbon* **2019**, *155*, 204–214. DOI: 10.1016/j.carbon.2019.08.052

23. Lei, G.; Cao, Y.; Zhao, W.; Dai, Z.; Shen, L.; Xiao, Y.; Jiang, L. Exfoliation of Graphitic Carbon Nitride for Enhanced Oxidative Desulfurization: A Facile and

General Strategy. *ACS Sustainable Chem. Eng.* **2019**, *7* (5), 4941–4950. DOI: 10.1021/acssuschemeng.8b05553

24. Lei, G.; Zhao, W.; Shen, L.; Liang, S.; Au, C.; Jiang, L. Isolated Iron Sites Embedded in Graphitic Carbon Nitride (gC3N4) for Efficient Oxidative Desulfurization. *Appl. Catal. B* **2020**, *267*, 118663. DOI: 10.1016/j.apcatb.2020.118663
25. Liao, G.; Gong, Y.; Zhang, L.; Gao, H.; Yang, G.-J.; Fang, B. Semiconductor Polymeric Graphitic Carbon Nitride Photocatalysts: The "Holy Grail" for the Photocatalytic Hydrogen Evolution Reaction Under Visible Light. *Energy Environ. Sci.* **2019**, *12* (7), 2080–2147. DOI: 10.1039/C9EE00717B
26. Ong, W. J.; Tan, L. L.; Ng, Y. H.; Yong, S. T.; Chai, S. P. Graphitic Carbon Nitride (g-C3N4)-Based Photocatalysts for Artificial Photosynthesis and Environmental Remediation: Are We a Step Closer to Achieving Sustainability? *Chem. Rev.* **2016**, *116* (12), 7159–7329. DOI: 10.1021/acs.chemrev.6b00075
27. Liao, G.; He, F.; Li, Q.; Zhong, L.; Zhao, R.; Che, H.; Gao, H.; Fang, B. Emerging Graphitic Carbon Nitride-Based Materials for Biomedical Applications. *Prog. Mater. Sci.* **2020**, *112*, 100666. DOI: 10.1016/j.pmatsci.2020.100666
28. Moniz, S. J. A.; Shevlin, S. A.; Martin, D. J.; Guo, Z.-X.; Tang, J. Visible-Light Driven Heterojunction Photocatalysts for Water Splitting-A Critical Review. *Energy Environ. Sci.* **2015**, *8* (3), 731–759. DOI: 10.1039/C4EE03271C
29. Xu, Y.; Kraft, M.; Xu, R. Metal-Free Carbonaceous Electrocatalysts and Photocatalysts for Water Splitting. *Chem. Soc. Rev.* **2016**, *45* (11), 3039–3052. DOI: 10.1039/c5cs00729a
30. He, B.; Feng, M.; Chen, X.; Zhao, D.; Sun, J. One-Pot Construction of Chitinderived Carbon/g-C3N4 Heterojunction for the Improvement of Visible-Light Photocatalysis. *Appl. Surf. Sci.* **2020**, *527*, 146737. DOI: 10.1016/j.apsusc.2020.146737
31. Fu, J.; Zhu, B.; Jiang, C.; Cheng, B.; You, W.; Yu, J. Hierarchical Porous ODoped g-C3N4 with Enhanced Photocatalytic CO2 Reduction Activity. *Small* **2017**, *13* (15), 1603938. DOI: 10.1002/smll.201603938
32. Jiang, Y.; Sun, Z.; Tang, C.; Zhou, Y.; Zeng, L.; Huang, L. Enhancement of Photocatalytic Hydrogen Evolution Activity of Porous Oxygen Doped g-C3N4

with Nitrogen Defects Induced by Changing Electron Transition. *Appl. Catal. B* **2019**, *240*, 30–38. DOI: 10.1016/j.apcatb.2018.08.059

33. Che, H.; Liu, C.; Che, G.; Liao, G.; Dong, H.; Li, C.; Song, N.; Li, C. Facile Construction of Porous Intramolecular gC3N4-Based Donor-Acceptor Conjugated Copolymers as Highly Efficient Photocatalysts for Superior H2 Evolution. *Nano Energy* **2020**, *67*, 104273. DOI: 10.1016/j.nanoen.2019.104273
34. Chen, X.; Shi, R.; Chen, Q.; Zhang, Z.; Jiang, W.; Zhu, Y.; Zhang, T. Threedimensional Porous g-C3N4 for Highly Efficient Photocatalytic Overall Water Splitting. *Nano Energy* **2019**, *59*, 644–650. DOI: 10.1016/j.nanoen.2019.03.010
35. Schwinghammer, K.; Mesch, M. B.; Duppel, V.; Ziegler, C.; Senker, J.; Lotsch, B. V. Crystalline Carbon Nitride Nanosheets for Improved Visible-Light Hydrogen Evolution. *J. Am. Chem. Soc.* **2014**, *136* (5), 1730–1733. DOI: 10.1021/ja411321s
36. Fontelles-Carceller, O. Mun˜ Oz-Batista, M.J., Ferna´ndez-Garcı´a, M, and Kubacka, A. *Interface Eff. Sunlight-Driven A.G. G-C*3N4 Composite Catalysts: Study of the Toluene Photodegradation Quantum Efficiency. ACS Appl. Mater. Interfaces **2016**, *8*, 2617–2627.
37. Xue, J.; Ma, S.; Zhou, Y.; Zhang, Z.; He, M. Facile Photochemical Synthesis of Au/ Pt/g-C3N4 with Plasmon-Enhanced Photocatalytic Activity for Antibiotic Degradation. *A.C.S. Appl. Mater. Interfaces* **2015**, *7* (18), 9630–9637. DOI: 10.1021/acsami.5b01212
38. Wang, X.-J.; Yang, W.-Y.; Li, F.-T.; Xue, Y.-B.; Liu, R.-H.; Hao, Y.-J. In Situ Microwave-Assisted Synthesis of Porous NTiO2/g-C3N4 Heterojunctions with Enhanced Visible-Light Photocatalytic Properties. *Ind. Eng. Chem. Res.* **2013**, *52* (48), 17140–17150. DOI: 10.1021/ie402820v
39. Wang, K.; Li, J.; Zhang, G. AgBridged Z-Scheme 2D/2D Bi5FeTi3O15/gC3N4 Heterojunction for Enhanced Photocatalysis: Mediator-Induced Interfacial Charge Transfer and Mechanism Insights. *A.C.S. Appl. Mater. Interfaces* **2019**, *11* (31), 27686–27696. DOI: 10.1021/acsami.9b05074
40. Low, J.; Yu, J.; Jaroniec, M.; Wageh, S.; Al-Ghamdi, A. A. Heterojunction Photocatalysts. *Adv. Mater.* **2017**, *29* (20), 1601694. DOI: 10.1002/adma.201601694

41. Zhou, H.; Qu, Y.; Zeid, T.; Duan, X.. Towards Highly Efficient Photocatalysts Using Semiconductor Nanoarchitectures. *Energy Environ. Sci.* **2012**, *5* (5), 6732. DOI: 10.1039/c2ee03447f
42. Marschall, R.. Semiconductor Composites: Strategies for Enhancing Charge Carrier Separation to Improve Photocatalytic Activity. *Adv. Funct. Mater.* **2014**, *24* (17), 2421–2440. DOI: 10.1002/adfm.201303214
43. Moniz, S. J. A.; Shevlin, S. A.; Martin, D. J.; Guo, Z.-X.; Tang, J.. Visible-Light Driven Heterojunction Photocatalysts for Water Splitting – A Critical Review. *Energy Environ. Sci.* **2015**, *8* (3), 731–759. DOI: 10.1039/C4EE03271C
44. Wang, H.; Zhang, L.; Chen, Z.; Hu, J.; Li, S.; Wang, Z.; Liu, J.; Wang, X.. Semiconductor Heterojunction Photocatalysts: Design, Construction, and Photocatalytic Performances. *Chem. Soc. Rev.* **2014**, *43* (15), 5234–5244. DOI: 10.1039/c4cs00126e
45. Hyun, J. K.; Zhang, S.; Lauhon, L. J.. Nanowire Heterostructures. *Annu. Rev. Mater. Res.* **2013**, *43* (1), 451–479. DOI: 10.1146/annurev-matsci-071312-121659
46. Hyun, J. K.; Zhang, S.; Lauhon, L. J.. Nanowire Heterostructures. *Annu. Rev. Mater. Res.* **2013**, *43* (1), 451–479. DOI: 10.1146/annurev-matsci-071312-121659
47. Li, K.; Gao, S.; Wang, Q.; Xu, H.; Wang, Z.; Huang, B.; Dai, Y.; Lu, J.. In-Situ-Reduced Synthesis of Ti^{3+} Self-Doped TiO_2/g-C_3N_4 Heterojunctions with High Photocatalytic Performance under LED Light Irradiation. *A.C.S. Appl. Mater. Interfaces* **2015**, *7* (17), 9023–9030. DOI: 10.1021/am508505n
48. Hong, S. J.; Lee, S.; Jang, J. S.; Lee, J. S.. Heterojunction BiVO4/WO3 Electrodes for Enhanced Photoactivity of Water Oxidation. *Energy Environ. Sci.* **2011**, *4* (5), 1781. DOI: 10.1039/c0ee00743a
49. Huang, L. Y.; Xu, H.; Li, Y. P.; Li, H. M.; Cheng, X. N.; Xia, J. X.; Xu, Y. G.; Cai, G. B.. Visible-Light-Induced WO3/g-C3N4 Composites with Enhanced Photocatalytic Activity. *Dalton Trans.* **2013**, *42* (24), 8606–8616. DOI: 10.1039/c3dt00115f
50. Pan, C.; Xu, J.; Wang, Y.; Li, D.; Zhu, Y.. Dramatic Activity of C 3 N 4 /BiPO 4 Photocatalyst with Core/Shell Structure Formed by Self-Assembly. *Adv. Funct. Mater.* **2012**, *22* (7), 1518–1524. DOI: 10.1002/adfm.201102306
51. Zhou, M. H.; Yu, J. G.; Liu, S. W.; Zhai, P. C.; Jiang, L.. Effects of Calcination Temperatures on Photocatalytic Activity of SnO2/TiO2 Composite Films

Prepared by an EPD Method. *J. Hazard. Mater.* **2008**, *154* (1–3), 1141–1148. DOI: 10.1016/j.jhazmat.2007.11.021

52. Ong, W.-J.; Putri, L. K.; Tan, L.-L.; Chai, S.-P.; Yong, S.-T.. Heterostructured AgX/g-C3N4 (X = Cl and Br) Nanocomposites via a Sonication-Assisted Deposition-Precipitation Approach: Emerging Role of Halide Ions in the Synergistic Photocatalytic Reduction of Carbon Dioxide. *Appl. Catal. B* **2016**, *180*, 530–543. DOI: 10.1016/j.apcatb.2015.06.053
53. Wang, S.; Yu, J. Tuning Electronic Properties of Silicane Layers by Tensile Strain and External Electric Field: A Firstprinciples Study. *Thin Solid Films* **2018**, *654*, 107–115. DOI: 10.1016/j.tsf.2018.03.061
54. Deng, Z.; Wang, X. Strain Engineering on the Electronic States of Two-Dimensional GaN/Graphene Heterostructure. *R.S.C. Adv.* **2019**, *9* (45), 26024–26029. DOI: 10.1039/c9ra03175h
55. Bai, Y.; Luo, G.; Meng, L.; Zhang, Q.; Xu, N.; Zhang, H.; Wu, X.; Kong, F.; Wang, B.. Single-Layer ZnMN2 (M = Si, Ge, Sn) Zinc Nitrides as Promising Photocatalysts. *Phys. Chem. Chem. Phys.* **2018**, *20* (21), 14619–14626. DOI: 10.1039/c8cp01463a
56. Edalati, K.; Fujiwara, K.; Takechi, S.; Wang, Q.; Arita, M.; Watanabe, M.; Sauvage, X.; Ishihara, T.; Horita, Z.. Improved Photocatalytic Hydrogen Evolution on Tantalate Perovskites CsTaO 3 and LiTaO 3 by Strain-Induced Vacancies. *A.C.S. Appl. Energy Mater.* **2020**, *3* (2), 1710–1718. DOI: 10.1021/acsaem.9b02197
57. Wang, G.; Zhou, F.; Yuan, B.; Xiao, S.; Kuang, A.; Zhong, M.; Dang, S.; Long, X.; Zhang, W. Strain-Tunable Visible-Light-Responsive Photocatalytic Properties of Two-Dimensional CdS/g-C3N4: A Hybrid Density Functional Study. *Nanomaterials* **2019**, *9* (2), 244. DOI: 10.3390/nano9020244
58. Dai, B.; Chen, Y.; Hao, S. M.; Huang, H.; Kou, J.; Lu, C.; Lin, Z.; Xu, Z. Sustainable Internal Electric Field for Enhanced Photocatalysis: From Material Design to Energy Utilization. *J. Phys. Chem. Lett.* **2020**, 11 (17), 7407–7416. DOI: 10.1021/acs.jpclett.0c00889.
59. Pan, J.; Zhang, W.; Xu, X.; Hu, J. The Mechanism of Enhanced Photocatalytic Activity for Water-Splitting of ReS2 by Strain and Electric Field Engineering. *R.S.C. Adv.* **2021**, *11* (37), 23055–23063. DOI: 10.1039/d1ra03821d

60. Chen, H.; Tan, C.; Zhang, K.; Zhao, W.; Tian, X.; Huang, Y. Enhanced Photocatalytic Performance of ZnO Monolayer for Water Splitting via Biaxial Strain and External Electric Field. *Appl. Surf. Sci.* **2019**, *481*, 1064–1071. DOI: 10.1016/j.apsusc.2019.03.105

61. Rahimi, K.; Moshfegh, A. Z. *Phys. Chem. Chem. Phys.*. Band Alignment Tuning of Heptazine-g-C3N4/g-ZnO vdW Heterostructure as a Promising Water-Splitting Photocatalyst **2021**, *23* (36), 20675–20685. DOI: 10.1039/d1cp02911h

62. Giannozzi, P.; Baroni, S.; Bonini, N.; Calandra, M.; Car, R.; Cavazzoni, C.; Ceresoli, D.; Chiarotti, G. L.; Cococcioni, M.; Dabo, I.; Dal Corso, A.; de Gironcoli, S.; Fabris, S.; Fratesi, G.; Gebauer, R.; Gerstmann, U.; Gougoussis, C.; Kokalj, A.; Lazzeri, M.; Martin-Samos, L.; Marzari, N.; Mauri, F.; Mazzarello, R.; Paolini, S.; Pasquarello, A.; Paulatto, L.; Sbraccia, C.; Scandolo, S.; Sclauzero, G.; Seitsonen, A. P.; Smogunov, A.; Umari, P.; Wentzcovitch, R. M. QUANTUM ESPRESSO: A Modular and Open-Source Software Project for Quantum Simulations of Materials. J. Phys. Condens. Matter 2009, 21 (39), 395502. DOI: 10.1088/0953-8984/21/39/395502

63. Perdew, J. P.; Burke, K.; Ernzerhof, M. Generalized Gradient Approximation Made Simple. *Phys. Rev. Lett.* **1996**, *77* (18), 3865–3868. DOI: 10.1103/PhysRevLett.77.3865

64. Jain, A.; Hautier, G.; Ong, S. P.; Moore, C. J.; Fischer, C. C.; Persson, K. A.; Ceder, G.. Formation Enthalpies by Mixing GGA and GGA + U Calculations. *Phys. Rev. B* **2011**, *84* (4), 045115. DOI: 10.1103/PhysRevB.84.045115

65. Deng, J.; Liu, N.; Guo, J.; Chen, X. Large Spin Gaps in the Half-Metals M N 4 (M =Mn, Fe, Co) with N 2 Dimers. *Phys. Rev. B* **2019**, *99* (18), 184409. DOI: 10.1103/PhysRevB.99.184409

66. Kleinman, L.; Bylander, D. M. Efficacious Form for Model Pseudopotentials. *Phys. Rev. Lett.* 1982, 48 (20), 1425–1428. DOI: 10.1103/PhysRevLett.48.1425

67. Monkhorst, H. J.; Pack, J. D. Special Points for Brillouin-Zone Integrations. *Phys. Rev. B* 1976, 13 (12), 5188–5192. DOI: 10.1103/PhysRevB.13.5188

68. Shwetharani, R.; Kapse, S.; Thapa, R.; Nagaraju, D. H.; Balakrishna, R. G. Dendritic Ferroselite (FeSe 2) with 2D Carbon-Based Nanosheets of rGO and g-C 3 N 4 as Efficient Catalysts for Electrochemical Hydrogen Evolution. *A.C.S. Appl. Energy Mater.* **2020**, *3* (12), 12682–12691. DOI: 10.1021/acsaem.0c02619

69. Liu, J. Origin of High Photocatalytic Efficiency in Monolayer g-C 3 N 4 /CdS Heterostructure: A Hybrid DFT Study. *J. Phys. Chem. C* **2015**, *119* (51), 28417–28423. DOI: 10.1021/acs.jpcc.5b09092

70. Grimme, S.; Ehrlich, S.; Goerigk, L. Effect of the Damping Function in Dispersion Corrected Density Functional Theory. *J. Comput. Chem.* **2011**, *32* (7), 1456–1465. DOI: 10.1002/jcc.21759

71. Clark, S. J.; Segall, M. D.; Pickard, C. J.; Hasnip, P. J.; Probert, M. I. J.; Refson, K.; Payne, M. C.
First Principles Methods Using CASTEP. *Z. Kristallogr. Cryst. Mater.* **2005**, *220* (5–6), 567–570. DOI: 10.1524/zkri.220.5.567.65075

72. Liu, J.; Hua, E. High Photocatalytic Activity of Heptazine-Based g-C3N4/SnS2 Heterojunction and Its Origin: Insights from Hybrid DFT. *J. Phys. Chem. C* **2017**, *121* (46), 25827–25835. DOI: 10.1021/acs.jpcc.7b07914

73. Li, Y.; Li, Y. Cai Yang a. *Chang-Ping B Li-Hua Gan CoO G-C*3N4 p-n heterojunction catalyst in-situ loading CoP for enhanced photocatalytic H2 evolution,Applied Surface Science **2023**, *639*, 158180. DOI:10.1016/j.apsusc.2023.158180

74. Hamam, K. J.; Alomari, M. I. A Study of the Optical Band Gap of Zinc Phthalocyanine Nanoparticles Using UV–Vis Spectroscopy and DFT Function. *Appl. Nanosci.* **2017**, *7* (5), 261–268. DOI: 10.1007/s13204-017-0568-9

75. Kroke, E.; Schwarz, M.; Horath-Bordon, E.; Kroll, P.; Noll, B.; Norman, A. D. Tri-s-Triazine Derivatives. Part I. From Trichloro-tri-s-Triazine to Graphitic C3N4 StructuresPart II: Alkalicyamelurates M3[C6N7O3], M = Li, Na, K, Rb, Cs, Manuscript in Preparation. *New J. Chem.* **2002**, *26* (5), 508–512. DOI: 10.1039/b111062b

76. Silva, A. M.; Rojas, M. I. Electric and Structural Properties of Polymeric Graphite Carbon Nitride (g-C3N4): A Density Functional Theory Study. *Computational and Theoretical Chemistry* 2016, 1098, 41–49. DOI: 10.1016/j.comptc.2016.11.004

77. Shwetharani, R.; Kapse, S.; Thapa, R.; Nagaraju, D. H.; Balakrishna, R. G. Dendritic Ferroselite (FeSe 2) with 2D Carbon-Based Nanosheets of rGO and g-C

3 N 4 as Efficient Catalysts for Electrochemical Hydrogen Evolution. *A.C.S. Appl. Energy Mater.* **2020**, *3* (12), 12682–12691. DOI: 10.1021/acsaem.0c02619

78. Du, A.; Sanvito, S.; Li, Z.; Wang, D.; Jiao, Y.; Liao, T.; Sun, Q.; Ng, Y. H.; Zhu, Z.; Amal, R.; Smith, S. C.. Hybrid Graphene and Graphitic Carbon Nitride Nanocomposite: Gap Opening, Electron-Hole Puddle, Interfacial Charge Transfer, and Enhanced Visible Light Response. *J. Am. Chem. Soc.* **2012**, *134* (9), 4393–4397. DOI: 10.1021/ja211637p

79. Lin, Y.; Wang, Q.; Ma, M.; Li, P.; Maheskumar, V.; Jiang, Z.; Zhang, R. Enhanced Optical Absorption and Photocatalytic Water Splitting of g-C3N4/TiO2 Heterostructure Through C&B Codoping: A Hybrid DFT Study. *Int. J. Hydrog. Energy* **2021**, *46* (14), 9417–9432. DOI: 10.1016/j.ijhydene.2020.12.114